




A regime beyond the Hall-Petch and inverse-Hall-Petch regimes in ultrafine-grained solids

Huijun Zhang ^{1✉}, Feng Liu ¹, Goran Ungar^{1,2}, Zhongyu Zheng³, Qingping Sun⁴ & Yilong Han ^{5,6✉}

The strength of polycrystal increases as the grain diameter l decreases, i.e. the Hall-Petch behaviour. This trend reverses at about $3 < l < 15$ nm, i.e. the inverse-Hall-Petch behaviour. How the grain size affects material's strength at $l < 3$ nm (~ 12 particles) remains unclear. Here our simulations use mixtures of soft and hard particles so that compression can continuously reduce l to merely a few particles, resulting in ultrafine-grained solids termed as glass-crystal composites. Beyond the conventional Hall-Petch strengthening and inverse-Hall-Petch softening, we observe a power-law strengthening at $l < 14$ particles as a result of the blockage of shear-banding by crystalline grains. Amorphous and crystalline regions accommodate shear strains via bond-breaking and collective rotation, respectively. Moreover, a polycrystal-glass transition occurs at $l = 14$ particles featured with peaks of various quantities, which deepens the understanding on softening-strengthening transition.

¹State Key Laboratory for Mechanical Behaviour of Materials, Shaanxi International Research Center for Soft Matter, School of Materials Science and Engineering, Xi'an Jiaotong University, Xi'an 710049, China. ²Department of Materials Science and Engineering, University of Sheffield, Sheffield, UK.

³Institute of Mechanics, Chinese Academy of Sciences, School of Engineering Science, University of Chinese Academy of Sciences, Beijing, China.

⁴Department of Mechanical and Aerospace Engineering, Hong Kong University of Science and Technology, Clear Water Bay, Hong Kong, China.

⁵Department of Physics, Hong Kong University of Science and Technology, Clear Water Bay, Hong Kong, China. ⁶Hong Kong University of Science and Technology Shenzhen Research Institute, Shenzhen 518057, China. ✉email: huijun@xjtu.edu.cn; yilong@ust.hk

Polycrystals are usually deformed via dislocation motion and grain boundary (GB) sliding. The former dominates when GB density is low, and the latter dominates in fine-grained polycrystals. Consequently, the flow stress σ_f increases as the mean grain diameter l decreases for large-grained polycrystals because GBs impede the dislocation-mediated plasticity. This Hall–Petch behaviour^{1–3} gives way to inverse Hall–Petch behaviour when grain size is reduced to around 10–15 nm, where the GB sliding dominates the plasticity and softens the materials^{4,5}. Recently, GBs are stabilised through relaxation and segregation⁶ or through high pressure⁷ so that the inverse Hall–Petch softening effect is staved off, and the Hall–Petch behaviour can extend to 3 nm⁷. However, the effect of grain diameter on material strength at $l < 3$ nm has been rarely explored because ultrafine-grained polycrystals are usually unstable and undergo grain coarsening⁸.

We expect that the inverse Hall–Petch softening^{4–6,9} breaks down, and a Hall–Petch-like strengthening restores in the ultrafine-grained regime (Fig. 1) because polycrystals will become amorphous solids (i.e. glasses) when grains are small enough^{9,10} and glasses usually exhibit higher strength than their polycrystalline counterparts^{11–13}. In contrast to polycrystal whose plasticity is controlled by dislocation motion (Hall–Petch) or GB sliding (inverse Hall–Petch)⁴, glass deforms and flows in the form of nanoscale shear band^{14–16}, which is due to the propagation of localised shear transformation zones (STZs)^{17–19}. To search for the expected strengthening regime and investigate its mechanism, solids with ultrafine crystalline grains are needed.

In recent years, nanocrystallites embedded in an amorphous matrix have attracted considerable interest because these materials possess advantages of both polycrystal and glass. For example, such structure can produce ultrahigh strength²⁰ and world-record fatigue resistance²¹ and thereby shows promising

applications^{21,22}. These materials are known as the dual-phase glass-crystal structure²⁰ or nanocomposite²¹, and lack of a standard terminology. Here, we call them glass-crystal composites (GCCs). How the grain size affects the strength of such material and whether the inverse Hall–Petch softening gives way to a strengthening behaviour in ultrafine-grained materials remain unclear.

Polycrystals and GCCs with mean grain diameter $l < 3$ nm are difficult to fabricate. In the previous study, we found that the grain size of a polycrystal composed of hard and soft particles (Fig. 2a–c) can be continuously reduced to a few particles by compression (Fig. 2d and Supplementary Figs. 1 and 2)¹⁰. This system provides an ideal platform to study whether the inverse Hall–Petch strengthening breaks down and a Hall–Petch-like strengthening restores in the finer-grained regime. The microstructure change in solids is difficult to resolve in situ because of the fast dynamics and localised nature of STZs^{11,15,23}, and thus it has primarily been studied by simulations^{24,25}.

Here, we perform the event-driven molecular dynamics simulation²⁶ on binary mixtures of hard and soft particles in two dimensions (see details in “Methods”) for which the continuously tunable grain size has been achieved¹⁰. The system is compressed from a single crystal to polycrystals and to GCCs with continuously decreasing of l (Supplementary Figs. 1, 2c), which enables us to study the strength of the ultrafine-grained regime and its microstructure change and mechanism. The grain diameter is usually in unit of particle number in simulations and nanometer in experiments. The diameter of a typical metallic atom, e.g. Cu or Ni^{4,7}, is about 0.25 nm. The measured stress–strain curves at different packing fraction ϕ and mixing ratio x , the flow stress σ_f and shear modulus K as a function of crystalline grain size all show not only the conventional Hall–Petch strengthening and inverse-Hall–Petch softening, but also a power-law strengthening in the ultrafine-grained regime. The mechanisms of the mechanical behaviours are analysed from the microstructural deformations upon shear. The observed softening–hardening transition in Fig. 1 coincides with the polycrystal–glass transition identified in the previous work¹⁰.

Results

Structures of the GCCs. The area fraction ϕ increases with pressure (see “Methods” and Supplementary Fig. 2a). At $\phi = 0.62$, a random mixture of soft and hard particles with the mixing ratio x : $(1 - x)$ forms a single crystal (Supplementary Fig. 1) because their sizes are the same. As pressure increases, more soft particles are compressed and more size mismatches are produced, which leads to amorphisation (Fig. 2d, e) with the reduced crystallinity X (Fig. 2f) and grain size N_g (Fig. 2g, h). X is the fraction of crystalline particles, and N_g is the mean number of particles per crystalline grain (see the definition in “Methods”). Figure 2e shows that hard particles are highly apt to participate in crystalline grains. For systems with large x , less hard particles are available for grain formation, thereby decreasing the crystallinity (Fig. 2f). The crystalline order of particle i is characterised by its bond-orientational order parameter ψ_{6i} (see details in “Methods”). $|\psi_{6i}| = 1$ for a perfect hexagonal lattice and is close to zero for a disordered structure. As ϕ increases (i.e. the grain size decreases in Fig. 2h), $\langle |\psi_{6i}| \rangle$ gradually decreases for hard particles but maintains constant for soft particles (Fig. 2i), demonstrating that the structure primarily changes near hard particles.

For binary systems, the chemical short-range order (SRO) is characterised by the Warren-Cowley parameter^{27,28}

$$\alpha_{AB} = 1 - \frac{Z_{AB}}{x_B Z_A}, \quad (1)$$

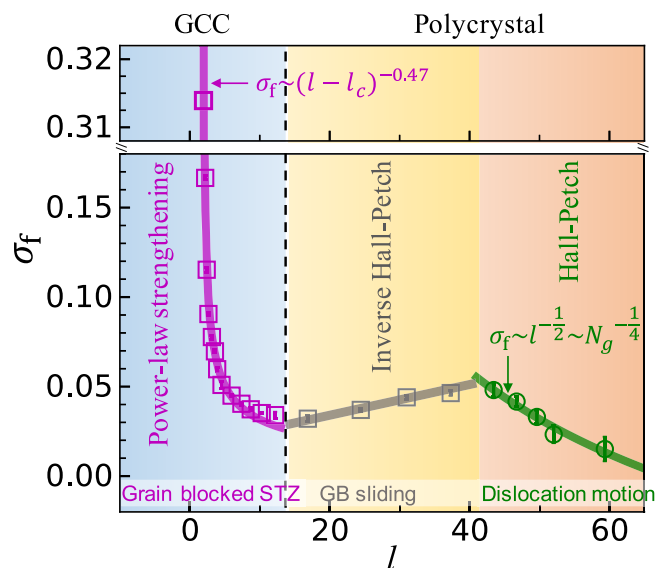


Fig. 1 Three regimes of flow stress $\sigma_f(l)$. As grain diameter l decreases, σ_f exhibits the Hall–Petch relationship (green curve) and the inverse Hall–Petch softening (grey line) in polycrystal regime^{1–6,10}, and a power-law strengthening (magenta curve) in the glass-crystal composite (GCC) regime. Symbols refer to the measured results at mixing ratio $x = 0.5$. The fitted $l_c = 1.89 \pm 0.01$. The boundary (dashed line) between the inverse Hall–Petch softening and power-law strengthening coincides with the polycrystal–glass transition (see Supplementary Note 1 for the details). The mechanisms of the three regimes: dislocation motion, grain boundary (GB) sliding, and grain blocked shear transformation zone (STZ) are shown in the bottom.

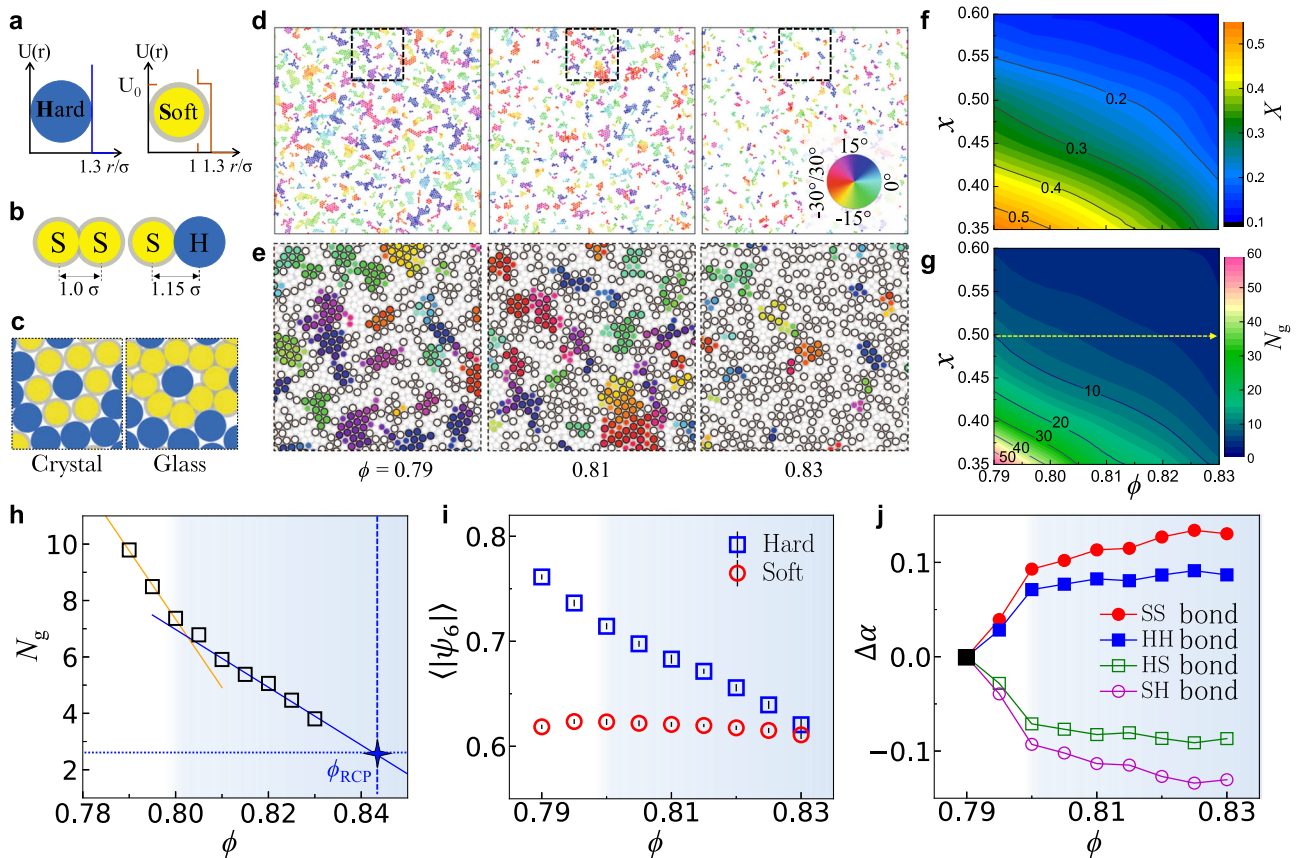


Fig. 2 Compression reduces the grain size in the glass-crystal composites (GCCs). **a** The interaction potentials for hard and soft particles. Soft particle has a square-shoulder potential with an outer diameter of 1.3 and inner hardcore diameter of 1. **b** Compressed bonds between soft-soft (SS) and soft-hard (SH) particles. **c** Example local packing structures for crystal (packing fraction $\phi = 0.65$) and glass ($\phi = 0.82$) without and with compressed bonds, respectively. **d** GCCs at different ϕ and mixing ratio $x = 0.5$. Each crystalline particle is coloured according to its angle of the bond-orientational order parameter ψ_6 as shown by the colour wheel. Disordered particles are in white. **e** The enlarged views of the dash-boxed regions in **d**. Crystallites (as coloured in **d**) are primarily composed of hard particles (black-rim circles). **f, g** The contour plots of crystallinity X and grain size N_g in the ϕ - x plane, respectively. Their colour bars are shown in the right. Three structural quantities at $x = 0.5$ are shown in **(h-j)**. **h** N_g decreases with ϕ . $N_g \approx 3$ when ϕ is extrapolated to the random close-packing density $\phi_{RCP} = 0.842$ for binary-disk systems⁶⁶. **i** $\langle |\psi_6| \rangle$ averaged over hard and soft particles. **j** $\Delta\alpha = \alpha(\phi) - \alpha(0.79)$ for four types of bonds, which reflect particles' aggregation propensity (Eq. (1)). The changes in slope at $\phi = 0.80$ in **(h, j)** correspond to a glass-glass transition (see Supplementary Note 2 for the details).

where Z_A is the coordination number of A-type particle; Z_{AB} is the number of B-type particles neighbouring surrounding A, and x_B is the fraction of B-type particles. $\alpha_{AB} = 0, >0$ and <0 correspond to random mixture, favoured, and unflavoured AB bonds, respectively. $\Delta\alpha$ of four types of bonds relative to the values at $\phi = 0.79$ (Fig. 2j) show that the same type particles have a higher affinity, which increases with ϕ . This demixing in binary solid can enhance the local packing efficiency²⁹ and result in a stable GCC.

Mechanical behaviours. The stress-strain curves at different ϕ in Fig. 3a exhibit a linear increase (i.e. elastic regime) at strain $\gamma < 0.025$ (Supplementary Fig. 3), a nonlinear increase (i.e. strain-hardening) at $0.025 < \gamma < 0.2$, and a plateau (i.e. steady flow) at $\gamma > 0.2$. The plateau height, which refers to the flow stress σ_f , increases as the grain size decreases at $N_g < 170$, i.e. $l \simeq \sqrt{170} \simeq 14$ particles. This behaviour is qualitatively different from the inverse Hall-Petch behaviour, and can neither be fitted by the Hall-Petch relationship^{1,2} (Fig. 3b). Instead, $\sigma_f(N_g)$ satisfies a power law,

$$\sigma_f(N_g) \propto (N_g - N_{g1})^{-\eta_1} \quad (2)$$

with the fitted $\eta_1 = 0.63 \pm 0.09$ and $N_{g1} = 3.24 \pm 0.17$ (Fig. 3b).

The shear modulus exhibits a similar power law

$$K(N_g) \propto (N_g - N_{g2})^{-\eta_2}, \quad (3)$$

with the fitted $\eta_2 = 0.72 \pm 0.14$ and $N_{g2} = 3.07 \pm 0.27$ (Fig. 3c). The σ_f and K diverge at $N_g \simeq 3$, indicating that the minimum grain size is at least 3 particles, which is consistent with the extrapolated N_g value at the random close-packing density in Fig. 2h where the stress diverges³⁰. The divergence is caused by the hard-core interactions between particles which render the system incompressible when the shells of soft particles collapse. Systems composed of soft-core particles can be infinitely compressed. In real systems, atoms exhibit hard cores under high pressures.

$\sigma_f(N_g)$ and $K(N_g)$ derived from the plastic and elastic regimes are strikingly similar. Thus $\sigma_f(K)$ is linear (Fig. 3c inset). This indicates that the solids with different grain sizes yield at the same strain, as confirmed in Supplementary Fig. 3 in which the slope of $\sigma_f(\gamma)$ always changes around $\gamma = 0.025$. The linear behaviour of $\sigma_f(K)$ is often observed in glasses^{28,31}.

The data for $x = 0.5$ in Fig. 3b and d are from different trials of simulation, and both well fit Eq. (2). $\sigma_f(N_g)$ at other mixing ratios can also be well fitted by Eq. (2) (Fig. 3d) and can collapse well onto the master line after being rescaled by the fitting parameters

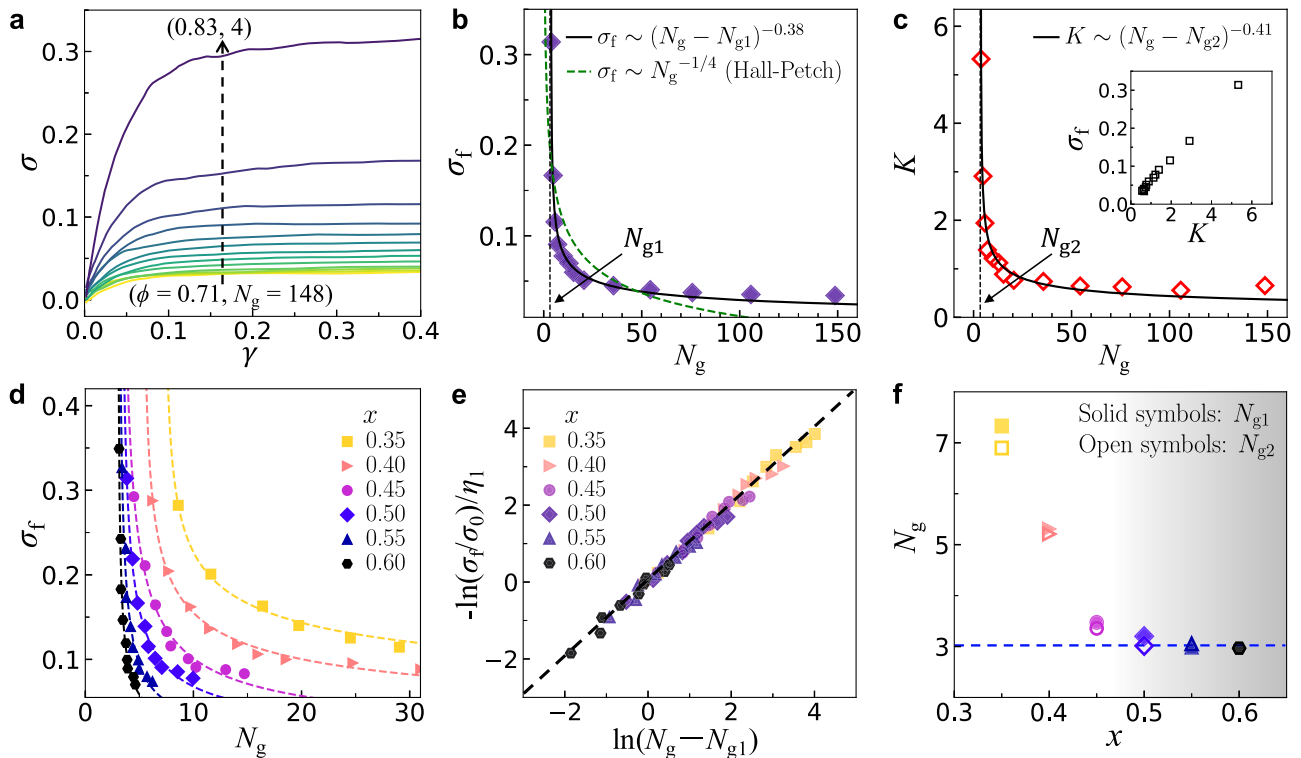


Fig. 3 Mechanical properties. **a** Stress-strain curves for glass-crystal composites (GCCs) with 50% soft particles at different packing fraction ϕ , corresponding to different grain size N_g . **b** The flow stress σ_f averaged over the strain range $0.3 < \gamma < 0.4$ in **(a)**. Black curve: the fitting of Eq. (2) with $N_{g1} = 3.24 \pm 0.17$ (vertical dashed line) and $\eta_1 = 0.63 \pm 0.09$. The Hall-Petch relation (green-dashed curve) cannot well fit the data. **c** The shear modulus K measured from the slope of $\sigma(\gamma)$ in the elastic regime of $\gamma < 0.025$ in **(a)**. Black curve: the fitting of Eq. (3) with $N_{g2} = 3.07 \pm 0.27$ and $\eta_2 = 0.72 \pm 0.14$. Inset: $\sigma_f(K)$. **d** σ_f fitted by Eq. (2) (dashed curves) at different x . **e** Rescaling of **(d)** collapses all the data on a straight line. **f** The fitted minimum grain sizes from $\sigma_f(N_g)$ (solid symbols) and $K(N_g)$ (open symbols) at different x .

(Fig. 3e). $K(N_g)$ at other mixing ratios also exhibit similar results as Fig. 3c. The minimum grain sizes $N_{g1,2}$ fitted from $\sigma_f(N_g)$ and $K(N_g)$ are very close and can be reduced to three particles when the fraction of soft particles $x \geq 0.5$ (Fig. 3f).

This power-law strengthening holds at $N_g < 170$ particles (Fig. 3b), i.e. $l < 3.5$ nm for typical alloys. At $l > 3.5$ nm, we observe the conventional inverse Hall-Petch behaviour, see section “Polycrystal-glass transition” for details. A similar inverse pseudo Hall-Petch to pseudo Hall-Petch transition has been recently reported at 3.1 nm in nanocrystalline graphene³², but there are only two data points at < 3.1 nm which can hardly provide a quantitative fitting.

Microstructure changes under shear. The structural deformation around particle i is characterised by the mean squared nonaffine displacement^{17,33},

$$D_i^2 = \frac{1}{N_i} \sum_{j=1}^{N_i} |\mathbf{d}_{ij} - \mathbf{F}_i \mathbf{d}_{ij}^0|^2 \quad (4)$$

which describes its neighbours’ average deviation from the linear strain field. $\mathbf{d}_{ij} = \mathbf{r}_j - \mathbf{r}_i$ is the distance vector between atom i and its neighbour j in the current state, \mathbf{d}_{ij}^0 is for the initial undeformed state, and \mathbf{F}_i is the transformation matrix for all distances between particle i and its N_i neighbours in a strain interval. Under shear (Fig. 4a–f), particles whose $D^2 > 0.6$ usually signature local plastic deformations³³, i.e. STZs, which are labelled in yellow in Fig. 4h–k. These yellow particles are mainly found in amorphous regions and anti-correlate with crystalline regions (Fig. 4o). The Pearson correlation coefficients between quantities A and B is defined as $C(A, B) = \frac{\langle \sum_i^N (A_i - \langle A \rangle)(B_i - \langle B \rangle) \rangle}{\sqrt{\langle \sum_i^N (A_i - \langle A \rangle)^2 \rangle} \sqrt{\langle \sum_i^N (B_i - \langle B \rangle)^2 \rangle}}$, where $\langle \rangle$ averages over all the

N particles. In the elastic regime $\gamma < 0.025$, plastic flows are absent (Fig. 4g). In the strain-hardening regime ($0.025 \leq \gamma \leq 0.2$), the high- D^2 yellow particles form small stripes with a typical thickness of 2–4 particles. These localised plastic flows, i.e. STZs, homogeneously occur in space (Fig. 4h–j) because scattered crystallites interrupt their growth (Fig. 4a–f and Supplementary Fig. 4b). By contrast, the plastic flows in normal glasses usually form extreme localised shear bands because no crystallite blocks the growth of STZs (Supplementary Fig. 4a). The extremely localised plastic flows in normal glasses often cause strain softening and even catastrophic failure, which limit their applications^{11,12}. By contrast, the homogeneous distribution of STZs in GCCs prevents the extreme localisation of plastic flow and leads to strain-hardening and associated strengthening effect (Fig. 3a, b)³⁴. As γ increases, the yellow deformation zones grow and percolate the whole sample (Fig. 4k and Supplementary Fig. 4c) in the steady flow regime $\gamma > 0.25$. Crystalline grains rotate (Fig. 4l), split (Fig. 4m), and rebuild (Fig. 4n) during the deformation process (see Supplementary Movies 1–3), which continuously affect the plastic flow.

Crystallites (high- $|\phi_c|$ regions) not only spatially anticorrelate with strong-local-rearrangement (large D^2) regions (Figs. 4o and 5a, b), but also tend to rotate clockwise, leading to more red clusters than blue clusters in Fig. 5c. This rotation is consistent with the shear direction. The long-live neighbour particles can characterize the local structural rearrangement and reflect the macroscopic rheological response of glasses from the microscopic structure³⁵. Such analysis has been applied in colloidal gel³⁶ and glass³⁵, but rarely in GCCs or polycrystals. We find that plastic flows with high D^2 (Fig. 5a) strongly correlate with particles having less long-lived neighbours (Fig. 5b). Crystalline particles have more long-lived neighbours than amorphous particles

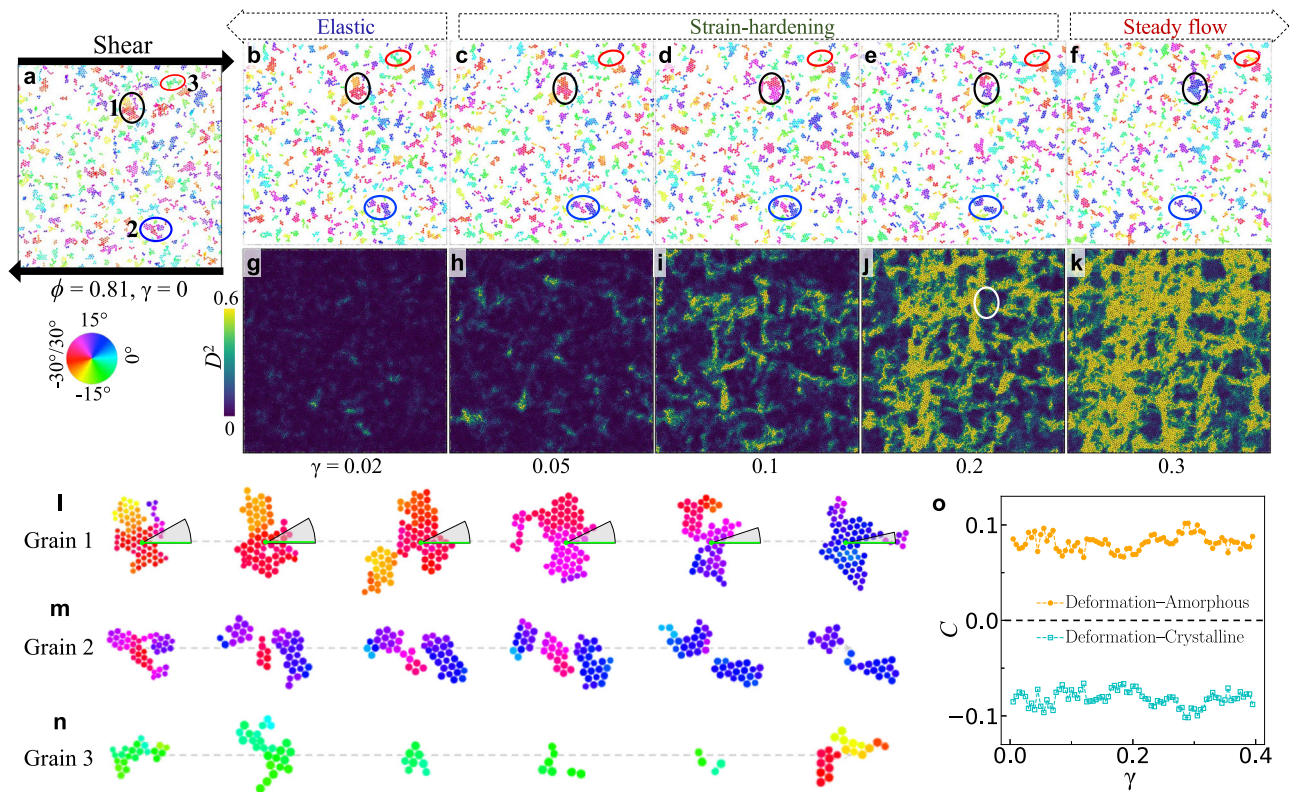


Fig. 4 Shear-induced deformations at packing fraction $\phi = 0.81$ with 50% soft particles. **a** The initial state without a strain. Black arrows denote the shear along the x direction. **b–f** The structures at $\gamma = 0.02, 0.05, 0.1, 0.2,$ and 0.3 , respectively. Crystalline particles are coloured in the same way as Fig. 2d. **g–k** Mean squared nonaffine displacements D^2 corresponding to (**b–f**), respectively. Particles strongly deviate from linear affine strain field are colour in yellow. The black (1), blue (2), and red (3) ellipses in (**a**) show crystalline grain that rotates (**l**), divides (**m**), and rebuilds (**n**) under shear, respectively. **l** The $[01]$ lattice direction of the crystalline grain in the black ellipses 1 in (**a–f**) rotates from 30° to 9° . This grain retains during the shear and impedes the spreading of STZ as shown by the white ellipse in (**j**). **m** A crystalline grain in the blue ellipses 2 in (**a–f**) disintegrates into two grains. **n** A crystalline grain becomes amorphous and then recrystallises into a new one in the red ellipses 3 in (**a–f**). **o** The Pearson correlation coefficients C between D^2 and crystalline order $|\psi_6|$ (squares) and between D^2 and disorderness $1 - |\psi_6|$ (circles).

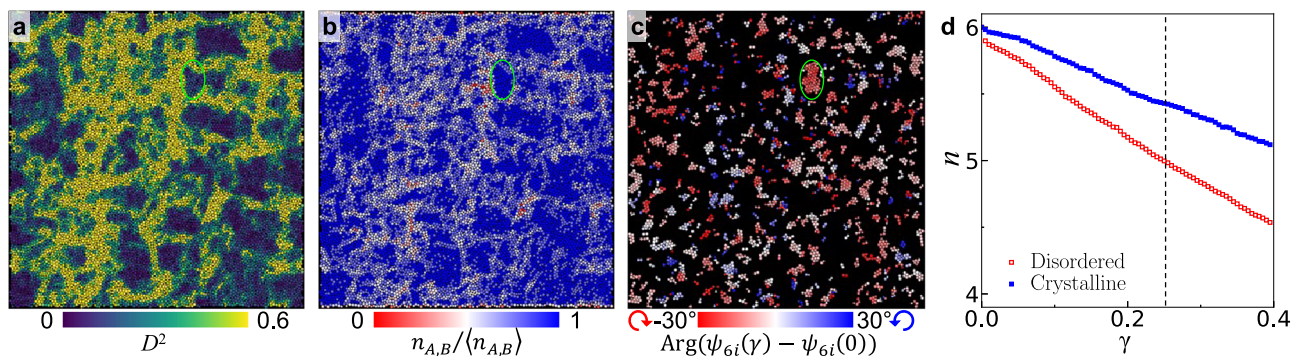


Fig. 5 Microstructure changes during plastic deformation at strain $\gamma = 0.25$. **a** The spatial distribution of nonaffine displacement D^2 . **b** The spatial distribution of the number of long-lived neighbours of each particle $n_{A,B}$ normalised by the average number $\langle n_{A,B} \rangle$, which anticorrelates with (**a**). **c** The rotation angle of crystalline particles when γ increases from 0 to 0.25. Clockwise rotations (red) dominate. Amorphous particles are in black. The green ellipses in (**a–c**) mark a crystalline grain that clockwise rotates (Fig. 4l) to accommodate the plastic flow. **d** The mean number of long-lived neighbours n for crystalline and disordered particles.

particularly at high γ (Fig. 5d), indicating that more bond breakings occur in amorphous regions. Since the plastic deformations mainly occur in amorphous regions, the yield strain is a constant regardless of the crystalline grain size (Fig. 3a and Supplementary Fig. 3).

The shear-induced structure changes are shown in Fig. 6. The average crystalline order $\langle |\psi_6| \rangle$ are nearly constant during plastic deformation (Fig. 6a). The average $\langle D^2 \rangle$ of soft particles are greater

than that of hard particles (Fig. 6b) and their ratio is constant in the plastic regime of $\gamma > 0.08$ (Fig. 6c), implying that a fixed large portion of deformation is obtained from the soft particles under shear. The deformation participation ratio $P_r = \frac{1}{N_{S,H}} \sum_i^{N_{S,H}} \Theta(D_i^2 - 0.6)$, where $N_{S,H}$ is the numbers of soft or hard particles and Θ is Heaviside function, i.e., the fraction of particles whose $D^2 > 0.6$. Soft particles show larger P_r than hard

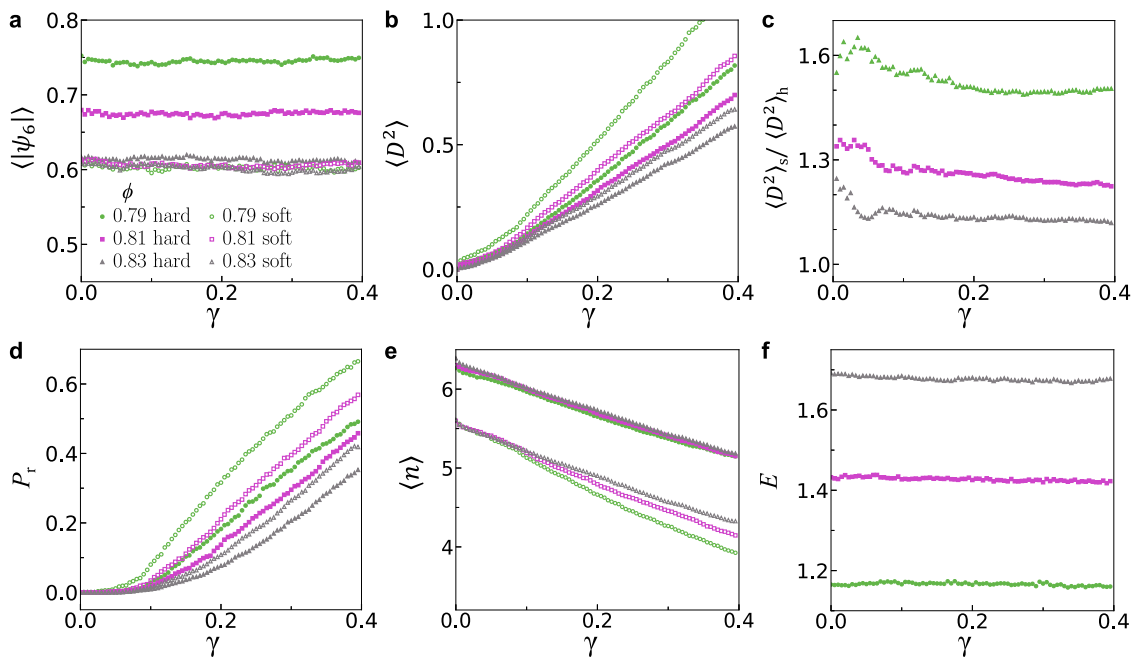


Fig. 6 Shear-induced changes for hard and soft particles at different packing fractions ϕ . **a** The average order parameter $\langle |\psi_{\phi}| \rangle$ for hard and soft particles remain constant during the deformation at each density. The legend in **(a)** is for panels **(a–f)**. **b** The average nonaffine displacement $\langle D^2 \rangle$ for hard and soft particles. **c** The ratio of $\langle D^2 \rangle$ for hard to soft particles. **d** Deformation participation ratios P_r ⁶⁷. **e** Mean number of long-lived neighbours n is insensitive to density for hard particles and more sensitive for soft particles as shear increases. n for soft particles are lower than that of hard particles because some soft particles are compressed smaller, and thus they have fewer neighbouring particles. **f** The average potential energy per particle under shear.

particles (Fig. 6d), which confirms their dominating contribution to plastic flows. The spatially uniform distribution of soft particles (Supplementary Fig. 1) accounts for the homogeneity of STZs (Fig. 4e–k and Supplementary Fig. 4b, c) that mitigate the extreme localisation of plastic flows (Supplementary Fig. 4a–c). The number of long-lived neighbouring particles $n(\gamma)$ at different ϕ or N_g are almost the same for hard particles, but different for soft particles (Fig. 6e). This finding is consistent with that shown in Fig. 5d, indicating that the plasticity mainly occurs on the soft particles distributed in amorphous regions (Fig. 2e). $n(\gamma)$ of soft particles decreases more rapidly in larger-grained GCCs (lower ϕ), implying that their local cages can be easily broken, and the stress can be effectively released. Therefore, large-grained GCCs show weaker strain-hardening and strengthening effects (Fig. 3b, d).

In contrast to strain softening in normal glasses, rejuvenated glasses exhibit strain-hardening similar to our GCCs because they both exhibit uniform flow stresses. However, we find that their underlying mechanisms are different. For rejuvenated glasses, the stored strain reduces the activation energy of STZ and causes uniform plastic flow with the decrease of energy³⁴. For GCCs, however, the crystallites block the shear banding, thereby producing a uniform plastic flow (Supplementary Fig. 4c) associated with a constant energy (Fig. 6f).

Polycrystal-glass transition. As grain size decreases small enough, a polycrystal or a GCC will eventually become an amorphous glass. It is not clear whether an ultrafine grained polycrystal or GCC should be called as polycrystal or amorphous glass, or it is just a matter of terminology without a clear distinction. This basic question has been rarely asked and poorly explored. Crystal-glass transition has been observed in colloidal^{37,38}, granular^{39,40}, and atomic systems^{41,42}, but these studies are neither about ultrafine-grained solids nor about the polycrystal-glass transition. Nanoindentation in Ni–W alloy

shows that the deformation morphology becomes similar to those in glasses when the grain size decreases to approximately 3 nm in the inverse Hall–Petch regimes⁹. However, whether this difference in deformation morphology indicates a polycrystal-to-glass transition remains unclear⁹. For the hard–soft binary systems, surprisingly we find that polycrystal–glass transition occurs at a sharp point rather than a gradual crossover¹⁰. Various quantities peak at $l \simeq 14$ particles, i.e. $\phi = 0.7$ (Supplementary Fig. 5)¹⁰, which indicates a sharp polycrystal-glass transition. Therefore, GCCs with $l < 14$ particles can also be considered as dual-phase glasses (Fig. 1). The polycrystal–glass transition coincides with the transition between the inverse Hall–Petch softening and the power-law strengthening regimes in Fig. 1. The maximum residual specific heat at $l = 14$ particles (Supplementary Fig. 5a) implies the maximum fluctuation of compressed SS or SH bonds, which is in accordance with the strongest fluctuations of structure and dynamics (Supplementary Fig. 5b, c). The maximum fluctuations of a structure parameter about crystallinity (Supplementary Fig. 5b) and a dynamic parameter about vibration amplitude (Supplementary Fig. 5c) at $l = 14$ particles imply the maximum compressibility as confirmed in Supplementary Fig. 5d, which is in accordance with the minimum strength at the boundary between the inverse Hall–Petch softening and power-law strengthening regimes (Fig. 1). Therefore, the features of the polycrystal–glass transition¹⁰ can explain the transition between the inverse Hall–Petch softening and the power-law strengthening. In turn, the transition provides an additional signature of the poorly explored polycrystal–glass transition.

The system can be compressed into a glass when $(x - 0.193)(0.786 - \frac{1}{\lambda}) > 0.02$ ¹⁰, i.e., the shoulder width λ and fraction of soft particles x must be large enough to provide sufficient size mismatches for glass formation. The power-law strengthening regime (Fig. 1) can exist only in samples whose λ and x satisfy the above inequality. For example, systems with small λ or x do not exhibit the strengthening regime because it is

a polycrystal instead of a glass even under the highest pressure (i.e. $\phi = 0.83$) in our simulation (see Supplementary Fig. 6).

The classical Hall–Petch strengthening and inverse Hall–Petch softening indicate that the strongest strength occurs at their boundary state. However, we observe the strength of GCCs can be six times higher than the boundary state between the Hall–Petch and inverse Hall–Petch regimes (Fig. 1). At $l \simeq 2$, $\sigma_f = 0.3$ in the reduced unit (Figs. 3b and 1) corresponds to $\sigma_f = 125$ GPa for graphene, whose energy and distance units are $U_0 = 525$ kJ mol⁻¹ and $\sigma = 0.128$ nm⁴³, respectively. Such σ_f is higher than the strength of polycrystal graphene^{32,44–46}. Therefore, the ultrafine-grained GCCs have the potential to achieve extremely high strength.

Discussion

Our simple system can model binary experimental systems whose components have different softness, such as alloys, granular and colloidal particles with different stiffness. For instance in Al–Ce alloy, the 4f-electrons of Ce atom are localised and thus Ce atoms interact via shoulder potentials⁴⁷, and their diameters can be reduced by 20% using cutting edge high-pressure technologies⁴⁸. Such large deformation is sufficient to induce the polycrystal–glass transition. In such binary systems, the grain size can be continuously decreased to a few particles because the size-mismatched particles, i.e. the compressed soft particles, are gradually ‘added’ through the interior of the bulk by compression¹⁰. It is well known that adding size-mismatched particles, i.e. solute particles, can reduce polycrystalline grain size⁸, but adding excessive solutes will produce glasses instead of ultrafine-grained polycrystal⁴⁹. By contrast, the solutes in our system are not added to the solution all at once, but incrementally added to the interior of the polycrystal, which hinders the glass formation. Thus, the soft–hard binary system provides a full spectrum of grain size, which bridges the polycrystal and glass and enables to explore how the strength changes with grain size beyond the Hall–Petch and inverse Hall–Petch regimes. We find that the inverse Hall–Petch softening terminates at $l \simeq 14$ particles, i.e. 3.5 nm in typical alloys, and a strengthening regime develops at $l < 14$ particles. The power-law strengthening regime in GCCs complements to the Hall–Petch and inverse Hall–Petch regimes for the grain size effect on solid strength (Fig. 1).

We observe that the strain-hardening and power-law strengthening arises from grain-mediated STZ, which is qualitatively different from the dislocation-mediated strengthening in the Hall–Petch relationship (Fig. 1). The uniformly distributed crystalline grains in the amorphous matrix impede the growth of STZs, which suppress the formation of extreme localised shear band. Therefore, GCCs avoid sudden stress drop that usually exists in normal glasses, and exhibit dramatic strengthening and strain-hardening which are absent in normal glasses. Moreover, we find that plastic deformation arises from bond-breaking in the amorphous regions and collective cluster rotation in the crystalline regions. Crystalline grain rotations often lead to good ductility, which explains the observed high ductility in dual-phase aluminium alloy²². This hardening mechanism avoids the inverse Hall–Petch softening in nanocrystal and the shear-band softening in glass, thereby providing a route to improve the strength of materials.

Low-dimensional systems are much softer because there are more long-wavelength fluctuations⁵⁰ and particles have fewer neighbour-provided constraints⁵¹. Consequently, the space dimension could affect the nature of phase transition such as crystal melting^{50,51} and glass dynamics⁵². For example, the transient localization of particles on approaching the glass transition is absent in 2D, but very pronounced 3D⁵². Analysis based

on local coordinates can avoid long-wavelength fluctuations so that the glassy behaviours are similar in 2D and 3D^{53–55}. We expect the strengthening beyond the inverse Hall–Petch (Fig. 1) remains valid in 3D because a completely disordered solid has a higher strength than the polycrystals in the inverse Hall–Petch regime in 3D. This expectation is independent of the dimensionality.

Various quantities of this binary system simultaneously peak at the same ϕ (Supplementary Fig. 5), which indicates a sharp polycrystal-to-glass transition point. In addition, we find that this polycrystal-glass transition point coincides with the transition between the inverse Hall–Petch softening and power-law hardening. The features at the polycrystal-glass transition can qualitatively explain the softening–hardening transition, and in turn, the softening–hardening transition provides an additional feature for the polycrystal-glass transition. The thermally induced transition and the nonequilibrium shear-induced transition are qualitatively different and the shear could shift the transition point. However, the polycrystal-glass transition without shear coincides with the softening–hardening transition with shear, which suggests deep connections between the material properties with and without shear. These results provide insights into the poorly explored polycrystal-glass transition and the discovered softening–hardening transition.

Methods

Model and simulation details. The soft particle is described by square-shoulder potential

$$U(r) = \begin{cases} \infty, & r \leq \sigma \\ U_0, & \sigma < r \leq \lambda\sigma \\ 0, & \lambda\sigma < r \end{cases} \quad (5)$$

where σ and $\lambda\sigma$ are the diameters of the inner hard core and outer shoulder, respectively. In this work, $\lambda = 1.3$. The energy unit U_0 is the height of the shoulder. The pair potential for hard particles is characterised as follows:

$$U(r) = \begin{cases} \infty, & r \leq \lambda\sigma \\ 0, & \lambda\sigma < r. \end{cases} \quad (6)$$

The square-shoulder potential has been used to describe cerium and cesium atoms, water and silica molecules, micelle and granular particles, and to study self-assembly, glasses, quasicrystals, and photonic crystals^{47,56–60}.

We simulate $N = 12,800$ particles under periodic boundary conditions with the fraction of soft particles x ranging from 0.35 to 0.6. The packing fraction ϕ is defined as the area fraction of hard particles and the hard cores of soft particles:

$$\phi = \frac{N\pi\sigma^2}{4A} [(1-x)\lambda^2 + x], \quad (7)$$

where A is the area of the simulation box. Particles are randomly distributed in a low-density fluid ($\phi = 0.5$) state and then relaxed at temperature $T = 2.0U_0/k_B$. The relaxed systems are then compressed into polycrystal and glass (Supplementary Fig. 1) by using the Lubachevsky–Stillinger algorithm⁶¹. The resultant systems are sufficiently equilibrated at $T = 0.13U_0/k_B$ for a time period of $10^5 t_0$, where k_B is the Boltzmann constant, $t_0 = \sqrt{m\sigma^2/U_0}$ is the mean time for a particle moving a distance σ , and m is the unit of mass for hard and soft particles. All the results are measured at $T = 0.13U_0/k_B$. After the system is compressed to the desired ϕ and its corresponding N_g , a shear is applied along the x direction by using the Lees–Edwards periodic condition in y direction with a strain rate of 10^{-5} . All figure and movies are about samples with 50:50 soft–hard mixing ratio. Samples with other mixing ratios range from 35:65 to 60:40 exhibit similar results. Each simulation is repeated ten times for sufficient statistics.

Identification of crystalline grains. The local hexagonal order of particle j is characterised by the weighted bond-orientational order parameter⁶²

$$\psi_{6j} = \frac{1}{l_{\text{tot}}} \sum_{k=1}^{N_j} l_{jk} e^{i6\theta_{jk}}, \quad (8)$$

where θ_{jk} is the orientational angle of the bond between particle j and its neighbour k . $i^2 = -1$. The Voronoi polygon has N_j edges with perimeter l_{tot} , and the length of the edge between j and k is l_{jk} . A higher $|\psi_{6j}|$ represents a higher 6-fold crystalline order. A crystalline bond is defined as $|\psi_{6j} \cdot \psi_{6k}^*| > 0.6$. A particle with three or more crystalline bonds is defined as a crystalline particle^{63,64}. Two neighbouring crystalline particles belong to the same grain if the difference between their

orientational angle is less than 6° . Non-crystalline particles and single isolated crystalline particles are defined as disordered.

The weighted mean grain size^{10,65}

$$N_g = \sum \frac{n_s s^2}{N_x}, \quad (9)$$

where n_s is the number of grains with s crystalline particles; N_x is the total number of crystalline particles; and $\frac{n_s s^2}{N_x}$ is the probability that a particle belongs to the s -sized grains. The grain diameter $l = \sqrt{N_g}$.

Data availability

All the data used in this work are available on reasonable request from the corresponding author.

Code availability

Computer codes used to generate the plots in this work are available upon reasonable request via email to H.Z.

Received: 7 April 2022; Accepted: 1 December 2022;

Published online: 15 December 2022

References

- Hall, E. O. The deformation and ageing of mild steel: III discussion of results. *Proc. Phys. Soc. London B* **64**, 747 (1951).
- Petch, N. J. The cleavage strength of polycrystals. *J. Iron Steel Inst.* **174**, 25–28 (1953).
- Cordero, Z. C., Knight, B. E. & Schuh, C. A. Six decades of the Hall–Petch effect—a survey of grain-size strengthening studies on pure metals. *Int. Mater. Rev.* **61**, 495–512 (2016).
- Schiøtz, J. & Jacobsen, K. W. A maximum in the strength of nanocrystalline copper. *Science* **301**, 1357–1359 (2003).
- Wu, J. et al. Mechanical instability of monocrystalline and polycrystalline methane hydrates. *Nat. Commun.* **6**, 8743 (2015).
- Hu, J., Shi, Y. N., Sauvage, X., Sha, G. & Lu, K. Grain boundary stability governs hardening and softening in extremely fine nanograined metals. *Science* **355**, 1292–1296 (2017).
- Zhou, X. et al. High-pressure strengthening in ultrafine-grained metals. *Nature* **579**, 67–72 (2020).
- Chookajorn, T., Murdoch, H. A. & Schuh, C. A. Design of stable nanocrystalline alloys. *Science* **337**, 951–954 (2012).
- Trelewicz, J. R. & Schuh, C. A. The Hall–Petch breakdown in nanocrystalline metals: a crossover to glass-like deformation. *Acta Mater.* **55**, 5948–5958 (2007).
- Zhang, H. & Han, Y. Compression-induced polycrystal-glass transition in binary crystals. *Phys. Rev. X* **8**, 041023 (2018).
- Schuh, C. A., Hufnagel, T. C. & Ramamurty, U. Mechanical behavior of amorphous alloys. *Acta Mater.* **55**, 4067–4109 (2007).
- Sun, B. A. & Wang, W. H. The fracture of bulk metallic glasses. *Prog. Mater. Sci.* **74**, 211–307 (2015).
- Sun, Y. H., Concustell, A. & Greer, A. L. Thermomechanical processing of metallic glasses: extending the range of the glassy state. *Nat. Rev. Mater.* **1**, 16039 (2016).
- Chen, H., He, Y., Shiflet, G. J. & Poon, S. J. Deformation-induced nanocrystal formation in shear bands of amorphous alloys. *Nature* **367**, 541–543 (1994).
- Greer, A. L., Cheng, Y. Q. & Ma, E. Shear bands in metallic glasses. *Mater. Sci. Eng. R Rep.* **74**, 71–132 (2013).
- Krisponeit, J.-O. et al. Crossover from random three-dimensional avalanches to correlated nano shear bands in metallic glasses. *Nat. Commun.* **5**, 3616 (2014).
- Falk, M. L. & Langer, J. S. Dynamics of viscoplastic deformation in amorphous solids. *Phys. Rev. E* **57**, 7192 (1998).
- Schall, P., Weitz, D. A. & Spaepen, F. Structural rearrangements that govern flow in colloidal glasses. *Science* **318**, 1895–1899 (2007).
- Puosi, F., Rottler, J. & Barrat, J.-L. Time-dependent elastic response to a local shear transformation in amorphous solids. *Phys. Rev. E* **89**, 042302 (2014).
- Wu, G., Chan, K.-C., Zhu, L., Sun, L. & Lu, J. Dual-phase nanostructuring as a route to high-strength magnesium alloys. *Nature* **545**, 80–83 (2017).
- Hua, P., Xia, M., Onuki, Y. & Sun, Q. Nanocomposite NiTi shape memory alloy with high strength and fatigue resistance. *Nat. Nanotechnol.* **16**, 409–413 (2021).
- Wu, G. et al. Hierarchical nanostructured aluminum alloy with ultrahigh strength and large plasticity. *Nat. Commun.* **10**, 5099 (2019).
- Wang, W. H. Dynamic relaxations and relaxation-property relationships in metallic glasses. *Prog. Mater. Sci.* **106**, 100561 (2019).
- Şopu, D., Stukowski, A., Stoica, M. & Scudino, S. Atomic-level processes of shear band nucleation in metallic glasses. *Phys. Rev. Lett.* **119**, 195503 (2017).
- Parmar, A. D. S., Kumar, S. & Sastry, S. Strain localization above the yielding point in cyclically deformed glasses. *Phys. Rev. X* **9**, 021018 (2019).
- Bannerman, M. N., Sargant, R. & Lue, L. Dynamo: a free general event-driven molecular dynamics simulator. *J. Comput. Chem.* **32**, 3329–3338 (2011).
- Warren, B. E. X-ray Diffraction (New York: Dover Publications Inc., 1990).
- Cheng, Y. Q. & Ma, E. Atomic-level structure and structure–property relationship in metallic glasses. *Prog. Mater. Sci.* **56**, 379–473 (2011).
- Nie, Y., Liu, J., Guo, J. & Xu, N. Connecting glass-forming ability of binary mixtures of soft particles to equilibrium melting temperatures. *Nat. Commun.* **11**, 3198 (2020).
- Jin, Y., Urbani, P., Zamponi, F. & Yoshino, H. A stability-reversibility map unifies elasticity, plasticity, yielding, and jamming in hard sphere glasses. *Sci. Adv.* **4**, eaat6387 (2018).
- Johnson, W. & Samwer, K. A universal criterion for plastic yielding of metallic glasses with a (t/t_g)^{2/3} temperature dependence. *Phys. Rev. Lett.* **95**, 195501 (2005).
- Han, J. The transition from an inverse pseudo hall-petch to a pseudo hall-petch behavior in nanocrystalline graphene. *Carbon* **161**, 542–549 (2020).
- Cao, P., Short, M. P. & Yip, S. Potential energy landscape activations governing plastic flows in glass rheology. *Proc. Natl. Acad. Sci. U.S.A.* **116**, 18790–18797 (2019).
- Pan, J., Ivanov, Y. P., Zhou, W. H., Li, Y. & Greer, A. L. Strain-hardening and suppression of shear-banding in rejuvenated bulk metallic glass. *Nature* **578**, 559–562 (2020).
- Laurati, M., Mafshoff, P., Mutch, K. J., Egelhaaf, S. U. & Zaccone, A. Long-lived neighbors determine the rheological response of glasses. *Phys. Rev. Lett.* **118**, 018002 (2017).
- Nabizadeh, M. & Jamali, S. Life and death of colloidal bonds control the rate-dependent rheology of gels. *Nat. Commun.* **12**, 4274 (2021).
- Zhao, K. & Mason, T. G. Frustrated rotor crystals and glasses of brownian pentagons. *Phys. Rev. Lett.* **103**, 208302 (2009).
- Yunker, P., Zhang, Z. & Yodh, A. G. Observation of the disorder-induced crystal-to-glass transition. *Phys. Rev. Lett.* **104**, 015701 (2010).
- Shen, H., Tong, H., Tan, P. & Xu, L. A universal state and its relaxation mechanisms of long-range interacting polygons. *Nat. Commun.* **10**, 1–8 (2019).
- Zhou, C.-C., Shen, H., Tong, H., Xu, N. & Tan, P. Coupling between particle shape and long-range interaction in the high-density regime. *Chin. Phys. Lett.* **37**, 086301 (2020).
- Deb, S. K., Wilding, M., Somayazulu, M. & McMillan, P. F. Pressure-induced amorphization and an amorphous–amorphous transition in densified porous silicon. *Nature* **414**, 528–530 (2001).
- Wang, Y.-C. et al. In situ tem study of deformation-induced crystalline-to-amorphous transition in silicon. *NPG Asia Materials* **8**, e291–e291 (2016).
- Bourque, A. J. & Rutledge, G. C. Empirical potential for molecular simulation of graphene nanoplatelets. *J. Chem. Phys.* **148**, 144709 (2018).
- Song, Z., Artyukhov, V. I., Yakobson, B. I. & Xu, Z. Pseudo Hall-Petch strength reduction in polycrystalline graphene. *Nano Lett.* **13**, 1829–1833 (2013).
- Sha, Z. D. et al. Inverse pseudo Hall-Petch relation in polycrystalline graphene. *Sci. Rep.* **4**, 5991 (2014).
- Chen, M. et al. Effects of grain size, temperature and strain rate on the mechanical properties of polycrystalline graphene – a molecular dynamics study. *Carbon* **85**, 135–146 (2015).
- Young, D. A. & Alder, B. J. Melting-curve extrema from a repulsive “step” potential. *Phys. Rev. Lett.* **38**, 1213–1216 (1977).
- Zeng, Q. S. et al. Long-range topological order in metallic glass. *Science* **332**, 1404–1406 (2011).
- T. Egami, Y. W. Atomic size effect on the formability of metallic glasses. *J. Non-Cryst. Solids* **64**, 113–134 (1984).
- Strandburg, K. J. Two-dimensional melting. *Rev. Mod. Phys.* **60**, 161 (1988).
- Wang, F., Zhou, D. & Han, Y. Melting of colloidal crystals. *Adv. Funct. Mater.* **26**, 8903–8919 (2016).
- Flenner, E. & Szamel, G. Fundamental differences between glassy dynamics in two and three dimensions. *Nat. Commun.* **6**, 7392 (2015).
- Shiba, H., Yamada, Y., Kawasaki, T. & Kim, K. Unveiling dimensionality dependence of glassy dynamics: 2d infinite fluctuation eclipses inherent structural relaxation. *Phys. Rev. Lett.* **117**, 245701 (2016).
- Vivek, S., Kelleher, C. P., Chaikin, P. M. & Weeks, E. R. Long-wavelength fluctuations and the glass transition in two dimensions and three dimensions. *Proc. Natl. Acad. Sci. U.S.A.* **114**, 1850–1855 (2017).

55. Illing, B. et al. Mermin–wagner fluctuations in 2d amorphous solids. *Proc. Natl. Acad. Sci. U.S.A.* **114**, 1856–1861 (2017).
56. Malescio, G. & Pellicane, G. Stripe phases from isotropic repulsive interactions. *Nat. Mater.* **2**, 97–100 (2003).
57. Osterman, N., Babič, D., Poberaj, I., Dobnikar, J. & Zihlerl, P. Observation of condensed phases of quasiplanar core-softened colloids. *Phys. Rev. Lett.* **99**, 248301 (2007).
58. Sperl, M., Zaccarelli, E., Sciortino, F., Kumar, P. & Stanley, H. E. Disconnected glass-glass transitions and diffusion anomalies in a model with two repulsive length scales. *Phys. Rev. Lett.* **104**, 145701 (2010).
59. Dotera, T., Oshiro, T. & Zihlerl, P. Mosaic two-lengthscale quasicrystals. *Nature* **506**, 208–211 (2014).
60. Pattabhiraman, H., Avvisati, G. & Dijkstra, M. Novel pyrochlorelike crystal with a photonic band gap self-assembled using colloids with a simple interaction potential. *Phys. Rev. Lett.* **119**, 157401 (2017).
61. Stillinger, F. H. & Lubachevsky, B. D. Crystalline-amorphous interface packings for disks and spheres. *J. Stat. Phys.* **73**, 497–514 (1993).
62. Mickel, W., Kapfer, S. C., Schröder-Turk, G. E. & Mecke, K. Shortcomings of the bond orientational order parameters for the analysis of disordered particulate matter. *J. Chem. Phys.* **138**, 044501 (2013).
63. Rein ten Wolde, P., Ruiz-Montero, M. J. & Frenkel, D. Numerical calculation of the rate of crystal nucleation in a lennard-jones system at moderate undercooling. *J. Chem. Phys.* **104**, 9932–9947 (1996).
64. Peng, Y. et al. Two-step nucleation mechanism in solid–solid phase transitions. *Nat. Mater.* **14**, 101–108 (2015).
65. Stauffer, D. & Aharony, A. *Introduction to Percolation Theory* (CRC press, 1994).
66. Desmond, K. W. & Weeks, E. R. Random close packing of disks and spheres in confined geometries. *Phys. Rev. E* **80**, 051305 (2009).
67. Shi, Y. & Falk, M. L. Strain localization and percolation of stable structure in amorphous solids. *Phys. Rev. Lett.* **95**, 095502 (2005).

Acknowledgements

We thank Zhibin Xu, Zhenwei Wu and Pengfei Guan for helpful discussions. This work was supported by the Fundamental Research Funds for the Central Universities (H.Z.: grant No. xxj032021001), the Key R&D Project of Shaanxi Province (H.Z.: grant No. 2022GY-400), the National Natural Science Foundation of China (H.Z.: grant No. 12274336), 111 Project 2.0 (G.U.: grant No. BP2018008), the Strategic Priority Research Program of the Chinese Academy of Sciences (Z.Z.: grant No. XDB22040301), the Guangdong Basic and Applied Basic Research Foundation (Y.H.: grant No. 2020B1515120067), and the Hong Kong Research Grants Council under the General Research Fund (Y.H.: grant No. CRF-C6016-20G, C6021-19EF).

Author contributions

H.Z. and Y.H. conceived the project. H.Z. performed the simulation and the data analyses. H.Z., F.L., G.U., Z.Z., Q.S. and Y.H. discussed the results and contributed to the explanations. H.Z. and Y.H. wrote the manuscript.

Competing interests

The authors declare no competing interests.

Additional information

Supplementary information The online version contains supplementary material available at <https://doi.org/10.1038/s42005-022-01107-7>.

Correspondence and requests for materials should be addressed to Huijun Zhang or Yilong Han.

Peer review information *Communications Physics* thanks the anonymous reviewers for their contribution to the peer review of this work. Peer reviewer reports are available.

Reprints and permission information is available at <http://www.nature.com/reprints>

Publisher's note Springer Nature remains neutral with regard to jurisdictional claims in published maps and institutional affiliations.



Open Access This article is licensed under a Creative Commons Attribution 4.0 International License, which permits use, sharing, adaptation, distribution and reproduction in any medium or format, as long as you give appropriate credit to the original author(s) and the source, provide a link to the Creative Commons license, and indicate if changes were made. The images or other third party material in this article are included in the article's Creative Commons license, unless indicated otherwise in a credit line to the material. If material is not included in the article's Creative Commons license and your intended use is not permitted by statutory regulation or exceeds the permitted use, you will need to obtain permission directly from the copyright holder. To view a copy of this license, visit <http://creativecommons.org/licenses/by/4.0/>.

© The Author(s) 2022